Sensors & Actuators: B. Chemical 346 (2021) 130495

Contents lists available at ScienceDirect

Sensors and Actuators: B. Chemical

journal homepage: www.elsevier.com/locate/snb

Dual-quenching electrochemiluminescence resonance energy transfer system from IRMOF-3 coreaction accelerator enriched nitrogen-doped GQDs to ZnO@Au for sensitive detection of procalcitonin

Lihua Hu [a,b,*], Cui Song [a,b], Tengfei Shi [a,b], Qianqian Cui [a,b], Lei Yang [a,b], Xiaojian Li [a,b], Dan Wu [a,b], Hongmin Ma [a,b], Yong Zhang [a,b], Qin Wei [a,b,*], Huangxian Ju [c]

[a] Collaborative Innovation Center for Green Chemical Manufacturing and Accurate Detection, School of Chemistry and Chemical Engineering, University of Jinan, Jinan 250022, China

[b] Key Laboratory of Interfacial Reaction & Sensing Analysis in Universities of Shandong, School of Chemistry and Chemical Engineering, University of Jinan, Jinan 250022, China

[c] Key Laboratory of Analytical Chemistry for Life Science, School of Chemistry and Chemical Engineering, Nanjing University, Nanjing 210023, China

ARTICLE INFO

Keywords:
ECL-RET
Coreaction accelerator
N-GQDs
Dual-quenching
MOF

ABSTRACT

Herein a novel electrochemiluminescence resonance energy transfer (ECL-RET) pair of isoreticular metal organic framework-3 (IRMOF-3) enriched nitrogen-doped graphene quantum dots (N-GQDs) luminescent material (N-GQDs@IRMOF-3@N-GQDs, donor) and Au nanoparticles modified zinc oxide nanorod (ZnO@Au, acceptor) were firstly designed to fabricate a dual-quenching sandwich-type ECL immunosensor for ultrasensitive analysis of procalcitonin (PCT). IRMOF-3 not only acted as a carrier for abundantly enriching luminescent N-GQDs by internal encapsulation and external decoration, but also a coreaction accelerator which could boost the transformation of persulfate ion $S_2O_8^{2-}$ to generate more anion radical $SO_4^{\bullet -}$, so as to promote the ECL emission of N-GQDs. Additionally, Au nanoparticles were loaded onto the ZnO nanorods through *in-situ* modification to obtain ZnO@Au, which was firstly applied as a dual-quencher of ECL signal. In the best test environment, a wide detection range from 0.0001 to 100 ng mL^{-1} was obtained and the limit of detection is 12.58 fg mL^{-1} (S/N = 3). With excellent reproducibility and sensitivity, the practical test consequence of PCT in human serum samples was satisfactory. These results suggested that this sensing system could provide a reference model for effective detection of disease markers in clinical medicine.

1. Introduction

Procalcitonin (PCT) is composed of protein and mainly secreted by thyroid C cells. Its concentration is very low in the heathy human body. However, when the patient is infected with bacteria, PCT will be released into the blood and the blood concentration of PCT will increase [1]. So PCT can usually be used as a marker for diagnosing infections [2–4]. With the extensive use of antibiotics, antibiotic resistance has become an inevitable problem in contemporary medicine. Researchers have found that PCT can be applied as an indicator to tailor antibiotic treatment to help reduce antibiotic resistance [5,6]. If the PCT content in the individual is below 0.25 ug L^{-1}, the use of antibiotics is not recommended. When it is above 0.25 ug L^{-1}, antibiotic treatments can be used by clinicians [7–9]. Therefore, sensitive measurement of minute amount of PCT is very helpful for early diagnosis of infections and slowing down the development of antibiotic resistance. The traditional methods for the detection of PCT, such as microfluidic immunoassay [10], fluorescence analysis [11], radioimmunoassay [12] and colloidal gold colorimetry [13], which usually have some disadvantages, such as long detection time or narrow detection range. Therefore, it is still urgent to explore new methods with the advantage of a rapid, simple, wide detection range and ultrasensitivity for detection of PCT.

Electrochemiluminescence resonance energy transfer (ECL-RET) is the most widely used method in the detection of biomolecules based on its unique advantages, such as undisturbed by scattered light, high sensitivity and low cost [14–16]. Nevertheless, this system has a great

* Corresponding authors at: Collaborative Innovation Center for Green Chemical Manufacturing and Accurate Detection, School of Chemistry and Chemical Engineering, University of Jinan, Jinan 250022, China.
E-mail addresses: hulihua1206@163.com (L. Hu), sdjndxwq@163.com (Q. Wei).

https://doi.org/10.1016/j.snb.2021.130495
Received 18 January 2021; Received in revised form 30 May 2021; Accepted 23 July 2021
Available online 24 July 2021

challenge about finding a well-overlapping ECL donor-acceptor pair [17]. ECL-RET method exists between a donor and an acceptor is realized by means of energy transfer at the nanoscale. In addition, ECL-RET requires an overlapping relationship between the ECL spectrum of the donor and the UV–vis absorption spectrum of the acceptor [18–20]. Luminescent graphene quantum dots (GQDs), marked as small-sized zero-dimensional nanomaterial, are composed of graphene [21,22]. Due to their tunable size [23–25], low toxicity and biocompatibility [26–28], GQDs were used a lot in biosensing, catalysis, drug delivery, and on the like [29–32]. However, GQDs show a low quantum yield due to lack of surface passivation [33,34]. The conductivity and electrochemical properties of GQDs can be effectively regulated by doping [35]. Among them, nitrogen atoms have been frequently used to prepare nitrogen-doped graphene quantum dots (N-GQDs) [36,37]. N-GQDs have many surface oxygen-containing groups, which can improve their water solubility and facilitate their combination with other materials [38]. Besides, N-GQDs have higher quantum yields and more active sites than those of GQDs [39]. However, compared with classical luminescent substances, N-GQDs still have weaker ECL signals. So, it is important to explore new strategies to improve their ECL signals.

Metal-organic framework materials (MOFs) are a kind of coordination polymer, which generally use inorganic metals as the combining site, and organic ligand as the support to constitute 3D extension in space [40–42]. Because of the huge specific surface area, good chemical stability, adjustable pore size and topological diversity [43,44], MOFs have attracted considerable interest in separation [45,46], drug delivery [47,48], catalysis [49,50], sensing [51,52] and so on. Herein, N-GQDs are not only encapsulated into the inside of isoreticular metal organic framework-3 (IRMOF-3), but also loaded on the surface of IRMOF-3 by van der Waals interaction or strong chemical interaction through oxygen-containing functional groups to obtain IRMOF-3 enriched N-GQDs luminescent material (N-GQDs@IRMOF-3@N-GQDs), which greatly enhances the loading amount of luminescent material and improves the ECL signal of the composite. In addition, IRMOF-3 can act as a co-reaction promoter and further strengthen the ECL intensity on account of that its organic ligand 2-amino terephthalic acid (2-NH_2-BDC) can facilitate the transformation of co-reactant $S_2O_8^{2-}$ into $SO_4^{\bullet-}$ [53].

Pure metal oxide nanoparticles (MO) typically exhibit weak absorption of visible light. For example, only when the wavelength is less than 387 nm, the light can be absorbed by titanium dioxide [54,55]. Therefore, a lot of research has been done to enhance the light capture capability of MO, including modification [56,57], dye sensitization [58], and doping [59,60] with noble metal (NM). When MO is combined with NM, the light absorption range of the wide band gap MO can be extended [61]. MO core and NM surface deposition are one of MO-NM nanostructures. In this work, Au nanoparticles modified zinc oxide nanorod (ZnO@Au) was prepared and firstly used as ECL-RET acceptor because of the large surface area and high stability [62]. The UV–vis absorption spectra of ZnO nanorod and ZnO@Au nanocomposite were discovered to overlap with the ECL emission spectrum of N-GQDs@IRMOF-3@N-GQDs, respectively. Therefore, both ZnO and ZnO@Au can effectively quench the emission of N-GQDs@IRMOF-3@N-GQDs. Moreover, the UV–vis absorption spectrum of ZnO@Au can overlap more area with the ECL emission spectrum of N-GQDs@IRMOF-3@N-GQDs compared with that of Au nanoparticles and ZnO nanorod, respectively. Therefore, ZnO@Au can achieve the double quenching effect on N-GQDs@IRMOF-3@N-GQDs emmission. Considering the above, a double quenching ECL immunosensor based on N-GQDs@IRMOF-3@N-GQDs as an illuminant and ZnO@Au as a double quencher were firstly constructed for sensitive detection of PCT. This study may provide new ideas for practical detection of other analytes.

2. Experimental section

2.1. Synthesis of N-GQDs@IRMOF-3@N-GQDs

N-GQDs@IRMOF-3@N-GQDs was prepared according to the literature with minor modification [53]. First, 0.2 g of PVP and 15 mg of N-GQDs (detailed synthetic method was shown in the supplementary material) were dispersed in a 40 mL mixed solution (DMF: ethanol = 3:2), while 68.9 mg of $Zn(NO_3)_2{\cdot}6H_2O$ and 16.5 mg of 2-NH_2-BDC were dispersed in 6 mL of DMF solution. These two solutions were mixed and stirred for 0.5 h, followed by transferring them to a 50 mL polytetrafluoroethylene autoclave and reacted for 20 h at 100 °C. Afterwards, the solution was separated by centrifugation with DMF for three times, and the obtained solid was vacuum-dried for 12 h to obtain N-GQDs encapsulated IRMOF-3 (N-GQDs@IRMOF-3). Then, 10 mg of N-GQDs were dispersed in 15 mL of ultrapure water, 1 mL of EDC (400 mM)/NHS (100 mM) were added and stirred for 1 h at 4 °C, then 15 mg of N-GQDs@IRMOF-3 were added and the mixture were stirred continuously. Subsequently, the solid was collected by centrifugation. After drying, the product N-GQDs@IRMOF-3@N-GQDs were dissolved in chitosan (2 mg mL^{-1}) and placed in a 4 °C refrigerator when not in use.

2.2. Preparation of ZnO@Au

ZnO@Au was synthesized on the basis of the reported method with slight modifications [63]. 50 mg of ZnO nanorods (detailed experimental steps were shown in the supplementary material) were dispersed into 65 mL of ultrapure water and reacted for half an hour. Then, 0.09 mmoL CTAB was dispersed in the above solution at 50 ℃. 1 mL of 2% $HAuCl_4$ was added after the above solution was cooled to room temperature. Then the solution color changed from yellow to purple when 15 mL of 0.7 mmoL $NaBH_4$ were added. Finally, solids were collected by multiple centrifugations and dried to obtain ZnO@Au.

2.3. The establishment of the sandwich-type ECL immunosensor

Scheme 1 showed a brief description of the assembly process of the sensor on glassy carbon electrode (GCE, 4 mm in diameter). At first, the electrode was buffed with Al_2O_3 powder and a mirror-like surface was obtained after being washed thoroughly by ultrapure water. After that 6 μL of N-GQDs@IRMOF-3@N-GQDs composites were coated on the GCE and air-dried. Next, 4 μL of EDC (0.01 mol L^{-1})/NHS (0.002 mol L^{-1}) was dropped onto the electrode and incubated for 1 h, followed by rinsing with ultrapure water to remove the unreacted EDC/NHS. After drying, the electrode was coated with 6 μL of Ab_1. The unbound Ab_1 was then carefully rinsed off with PBS (pH 7.4). The modified electrode was further coated with 0.1 wt% BSA to take up the nonspecific site. Washing with PBS was also required after drying. Later on, the modified electrode was incubated with different concentrations PCT (6 μL) for 1 h at 4 °C and then the unbound antigen was similarly washed off with PBS. Finally, the ZnO@Au-Ab_2 (6 μL) was added to the electrode surface, and then rinsed with PBS once the electrode surface was dried. The ECL immunosensor (GCE/N-GQDs@IRMOF-3@N-GQDs/Ab_1/BSA/PCT/ZnO@Au-Ab_2) was obtained and kept at 4 °C.

2.4. ECL detection

10 mL of pH 8.0 PBS with 0.1 M KCl and 0.1 M $K_2S_2O_8$ were selected as the co-reactant system for ECL measurements. The reference electrode-Ag/AgCl electrode, the counter electrode-platinum wire electrode and the prepared working electrode were connected to the chemiluminescence detector's chamber as the electrochemical luminescence sensor. The electrochemical workstation and chemiluminescence detector were connected together. The high voltage of the photomultiplier tube was set as 800 V, and the scanning voltage was set as −1.6 ~ 0 V.

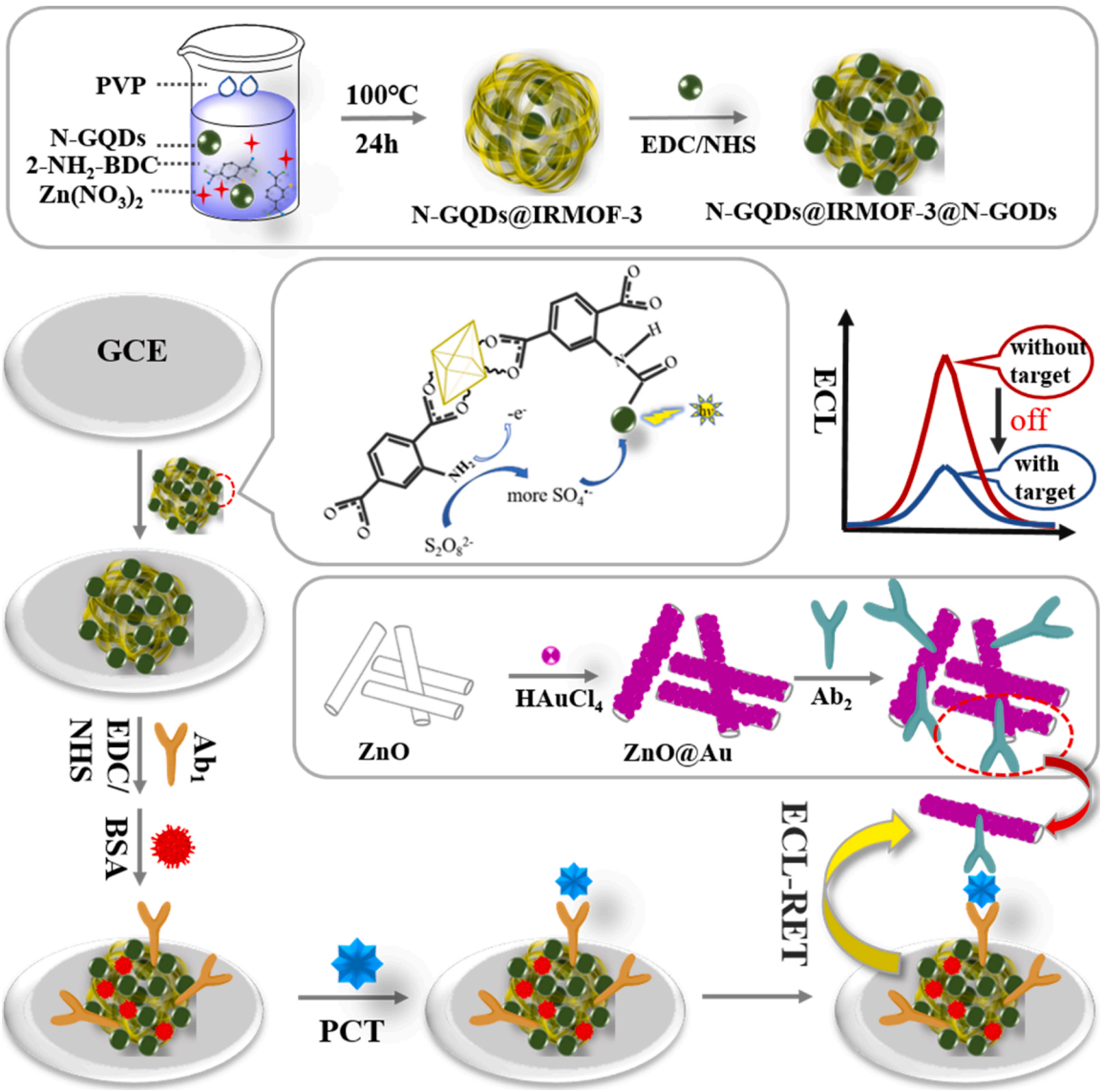

Scheme 1. Fabrication process of the proposed ECL immunosensor.

3. Results and discussion

3.1. Characterization of the prepared materials

Transmission electron microscopy (TEM) and scanning electron microscopy (SEM) technologies were applied to characterize the morphology and size of the synthesized materials. Representative results were exhibited in Fig. 1. In Fig. 1A, the N-GQDs have a uniform distribution, and its average size was less than 10 nm. Meanwhile, the inside high resolution TEM (HRTEM) image of N-GQDs showed a regular lattice structure. 0.21 nm of lattice spacing was consistent with a previous report [64]. Fig. 1B and C were scanning electron micrograph and transmission electron micrograph of IRMOF-3, respectively. As can be seen, the IRMOF-3 was a sphere structure with a diameter of about 500 ± 50 nm [65]. When N-GQDs were encapsulated into the inside of the IRMOF-3 (Fig. 1D), there was no obvious size change compared with that of the pure IRMOF-3. N-GQDs@IRMOF-3 still exhibited well-demarcated spherical structure and good dispersion. In addition, the enlarged TEM image of individual N-GQDs@IRMOF-3 shown in Fig. 1E further verified the encapsulation of the N-GQDs. Fig. 1F showed that the globular surface of the N-GQDs@IRMOF-3@N-GQDs were covered with lots of dots. Meantime, from the HRTEM image (Fig. 1G), the well lattice planes of N-GQDs can be clearly found on the outer shell of N-GQDs@IRMOF-3@N-GQDs, meaning N-GQDs have been successfully functionalized onto the outer shell of N-GQDs@IRMOF-3@N-GQDs. In addition, the results of high angle annular dark field-scanning transmission electron microscopy (HAADF-STEM) image and energy dispersive spectroscopy (EDS) mapping of N-GQDs@IRMOF-3@N-GQDs further confirmed the successful preparation of N-GQDs@IRMOF-3@N-GQDs (Fig. S1 in supplementary material). The scanning electron micrograph in Fig. 1H showed that the prepared ZnO nanomaterial had a rod-like nanostructure with a slippy surface. The average diameter of ZnO was about 150 nm and the axial length was nearly 500 nm. In contrast, the surface of the ZnO@Au were rough, uneven and covered by apparent protrusions, manifesting that Au nanoparticles were uniformly dispersed on the ZnO surface (Fig. 1I). Fig. S2 in supplementary material showed the EDS of ZnO@Au. The existence of Au, O, and Zn elements further confirmed that ZnO@Au nanocomposites were successfully synthesized (Fig. S2 in supplementary material). In addition, the TEM images of ZnO and ZnO@Au were shown in Fig. S3 in supplementary material. It can be seen that a lot of Au nanoparticles with a diameter of approximately 5–10 nm were successfully loaded onto the surface of ZnO.

The functional groups of the prepared materials were analyzed by

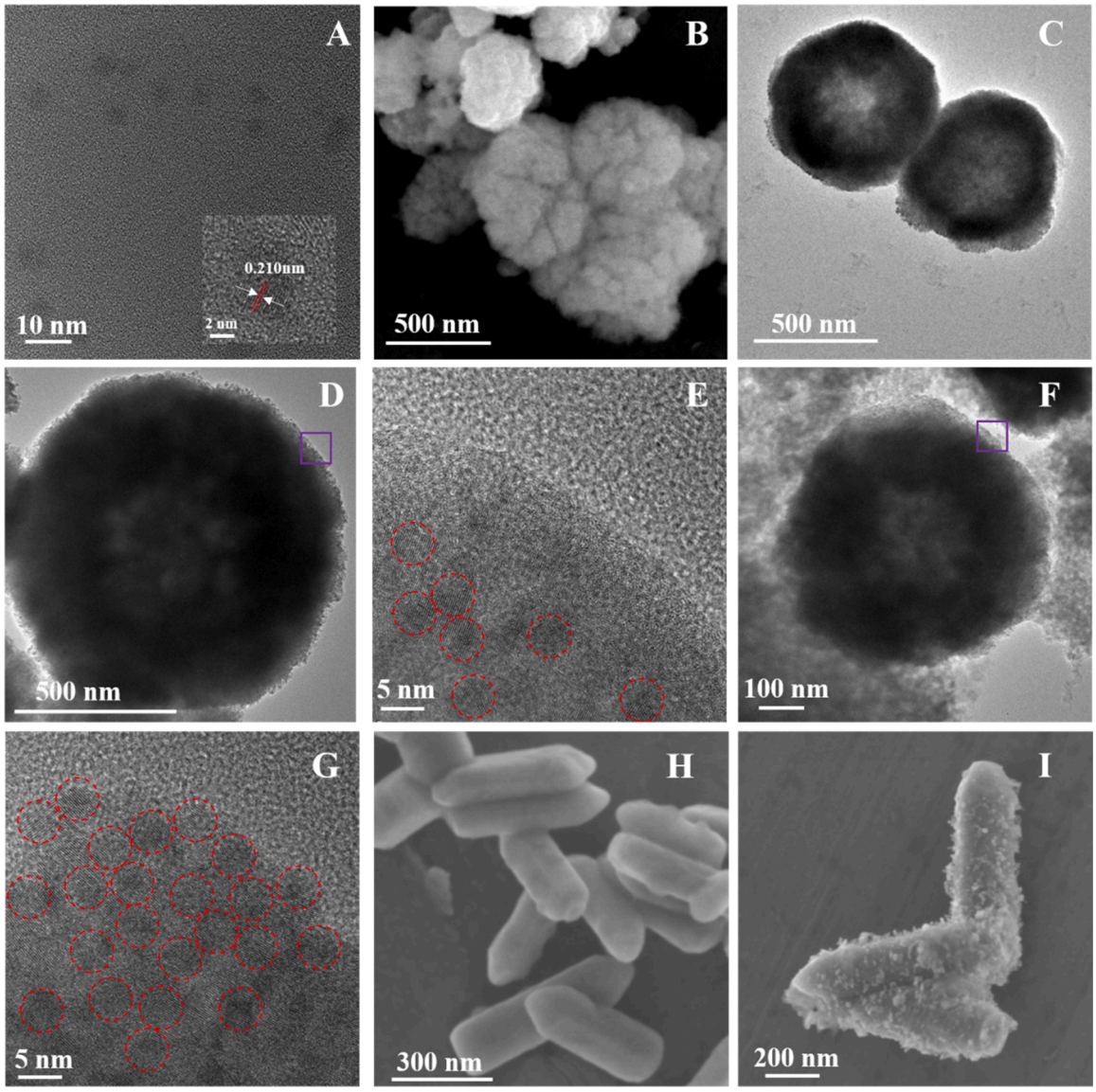

Fig. 1. TEM image of N-GQDs (A), SEM (B) and TEM (C) images of IRMOF-3 (C), TEM image of N-GQDs@IRMOF-3 (D), HRTEM image of individual N-GQDs@IRMOF-3 from the marked region in D (E), TEM image of N-GQDs@IRMOF-3@N-GQDs (F), HRTEM image of individual N-GQDs@IRMOF-3@N-GQDs from the marked region in F (G), SEM images of ZnO (H) and ZnO@Au (I).

Fourier transform infrared (FTIR) method (Fig. S4A in supplementary material). For N-GQDs (line a), C═O stretching vibration band can be found at 1675 cm^{-1}. C═C stretching vibration band can be found at 1538 cm^{-1}. Two vibration bands at 1304 cm^{-1} and 1374 cm^{-1} were observed, which can be assigned to the C—N bond vibration. The existence of alkyl groups, carboxyl groups and amino groups on N-GQDs can be speculated from the stretching of C—H, O—H and N—H at about 2640–3400 cm^{-1}. The asymmetric and symmetric stretching vibrations of NH_2 in the FTIR spectrum of IRMOF-3 can be found at 483 cm^{-1} and 3365 cm^{-1}, respectively. The existence of C—C in the benzene ring, C—N and C—O can be verified from the characteristic peaks at 1576 cm^{-1}, 1377 cm^{-1} and 1252 cm^{-1}, respectively (line b). Compared with that of the pure IRMOF-3, due to the N-GQDs in N-GQDs@IRMOF-3 were wrapped inside the IRMOF-3, and the peak position and intensity of N-GQDs@IRMOF-3 spectrum have not changed much (line c). This might be due to that the encapsulation amount of N-GQDs was relatively small. In the N-GQDs@IRMOF-3@N-GQDs spectrum, three main bands at around 1380 cm^{-1}, 1600 cm^{-1} and 3300 cm^{-1} became broader and nearly unification, which can be attributed to that many N-GQDs were covered on the outer-surface of N-GQDs@IRMOF-3@N-GQDs, and the typical groups of IRMOF-3 and N-GQDs were similar in structure, leading to the infrared absorption peaks overlapped with each other.

In order to demonstrate whether the nanoparticles were successfully prepared, X-ray diffraction (XRD) was further measured. The XRD pattern of N-GQDs was displayed in Fig. S4B in supplementary material. A broad peak at about 26.5° was (002) plane, whose *d* value of 0.389 nm was nearly the same as that of graphene [66]. The XRD pattern of IRMOF-3 was displayed in Fig. S4C in supplementary material, and the diffraction peaks at 6.9°, 9.8° and 13.97° correspond to (200), (220) and (400) planes, respectively [67]. The lower line in Fig. S4D in supplementary material was the ZnO pattern. A hexagonal wurtzite structure of ZnO can be indexed from the lattice parameters, which were consistent with the JCPDS-36-1451 file of ZnO [68]. The upper line was the XRD curve of ZnO@Au. The additional peaks at 38.37°, 44.24°,64.57° and 77.54° respectively corresponded to (111), (200), (220) and (311) planes of Au, indicated that Au NPs were Face Centered Cubic (FCC) phase, which corresponded to the file JCPDS NO: 4-0784.

3.2. ECL emission mechanism of N-GQDs/IRMOF-3/$K_2S_2O_8$ ternary system and the quenching mechanism of ZnO@Au

ECL emission mechanism of N-GQDs/IRMOF-3/$K_2S_2O_8$ ternary system was explored through ECL and CV measurements. In Fig. 2A, curve a and curve b were the ECL emission spectra of GCE and IRMOF-3 in $K_2S_2O_8$ solution, respectively. The maximum emission wavelength of curve a and curve b was both at 575 nm, which could be assigned to the emission of $^1(O_2)_2$* in the $O_2/S_2O_8^{2-}$ system [69]. The emission intensity of curve b was stronger than that of curve a, which indicated that IRMOF-3 may promote the ECL emission of the $O_2/S_2O_8^{2-}$ system. The curves of c and d were the ECL emission result of N-GQDs and N-GQDs@IRMOF-3@N-GQDs in $K_2S_2O_8$ solution, respectively, and both the maximum emission wavelength were at about 640 nm, indicating that the dominant luminescent substance in the N-GQDs/$K_2S_2O_8$ system were N-GQDs with $K_2S_2O_8$ as the coreactant. Corresponding ECL signals were shown in Fig. 2B. Line a and line b were the ECL responses of N-GQDs and N-GQDs@IRMOF-3 in PBS solution without $K_2S_2O_8$, respectively. It was shown that the ECL signal of both N-GQDs and N-GQDs@IRMOF-3 were weak. However, the ECL intensity of N-GQDs-modified GCE was obviously increased when measured in PBS solution with $K_2S_2O_8$, meaning $K_2S_2O_8$ played the role of coreactant of N-GQDs (Fig. 2B, line c). It's worth noting that When N-GQDs were wrapped inside the IRMOF-3 to form N-GQDs@IRMOF-3 composite, the ECL signal tested in PBS solution with $K_2S_2O_8$ was significantly enhanced (Fig. 2B, line d), which revealing that IRMOF-3 can promote the ECL emission of N-GQDs/$K_2S_2O_8$ system. In addition, the ECL signal of N-GQDs@IRMOF-3@N-GQDs modified electrode (Fig. 2B, line e) was further strengthened. It was due to more N-GQDs were combined with IRMOF-3 in N-GQDs@IRMOF-3@N-GQDs to produce higher ECL intensity. Similarly, the CV responses of electrodes with different modifications under different conditions were further tested to deeply investigate the effect of IRMOF-3 in the N-GQDs/$K_2S_2O_8$ system. It can be seen from Fig. S5 in supplementary material, IRMOF-3 showed an oxidation peak at $E_{p,a} = -1.11$ V and N-GQDs showed a reduction peak at $E_{p,a} = -0.97$ V in PBS solution without $K_2S_2O_8$. When N-GQDs and IRMOF-3 were combined together, the peak current of N-GQDs@IRMOF-3@N-GQDs did not show significant change, indicating that IRMOF-3 did not react with N-GQDs directly. However, when the modified electrodes were tested in PBS solution with $K_2S_2O_8$, the CV curves behaved differently from the above results. As shown in Fig. 2C, when IRMOF-3 was coated on the GCE, the reduction peak of $K_2S_2O_8$ shifted negatively and the peak current increased compared with those of pure GCE, meaning IRMOF-3 can boost $S_2O_8^{2-}$ to generate more $SO_4^{\bullet -}$ [70]. Moreover, the reduction peak of N-GQDs in $K_2S_2O_8$ solution was at −1.29, which was offset in a negative direction compared to the CV of N-GQDs tested without $K_2S_2O_8$. Actually, the interaction between $K_2S_2O_8$ and N-GQDs resulted in this increased overpotential. Finally, when IRMOF-3 was combined with N-GQDs, the peak current of N-GQDs@IRMOF-3@N-GQDs in PBS solution containing $K_2S_2O_8$ increased significantly, which further demonstrated that IRMOF-3 may accelerate the reaction between N-GQDs and $K_2S_2O_8$.According to the above, IRMOF-3 might be concluded as the coreaction accelerator, who can effectively enhance the ECL emission of N-GQDs/ $K_2S_2O_8$ system through interacting with $K_2S_2O_8$ rather than N-GQDs. The possible mechanisms of the new ternary ECL system are proposed as follows:

$$\text{IRMOF-3} - e^- \rightarrow \text{IRMOF-3}^{\bullet +} \quad (1)$$

$$\text{IRMOF-3}^{\bullet +} - H^+ \rightarrow \text{IRMOF-3}^{\bullet} \quad (2)$$

$$S_2O_8^{2-} + \text{IRMOF-3}^{\bullet} \rightarrow \text{IRMOF-3}^{+} + SO_4^{\bullet -} \quad (3)$$

$$S_2O_8^{2-} + e^- \rightarrow SO_4^{2-} + SO_4^{\bullet -} \quad (4)$$

$$\text{N-GQDs} + e^- \rightarrow \text{N-GODs}^{\bullet}\text{-} \quad (5)$$

$$\text{N-GQDs}^{\bullet -} + SO_4^{\bullet -} \rightarrow SO_4^{2-} + \text{N-GQDs*} \quad (6)$$

$$\text{N-GQDs*} \rightarrow \text{N-GQDs} + h\nu \quad (7)$$

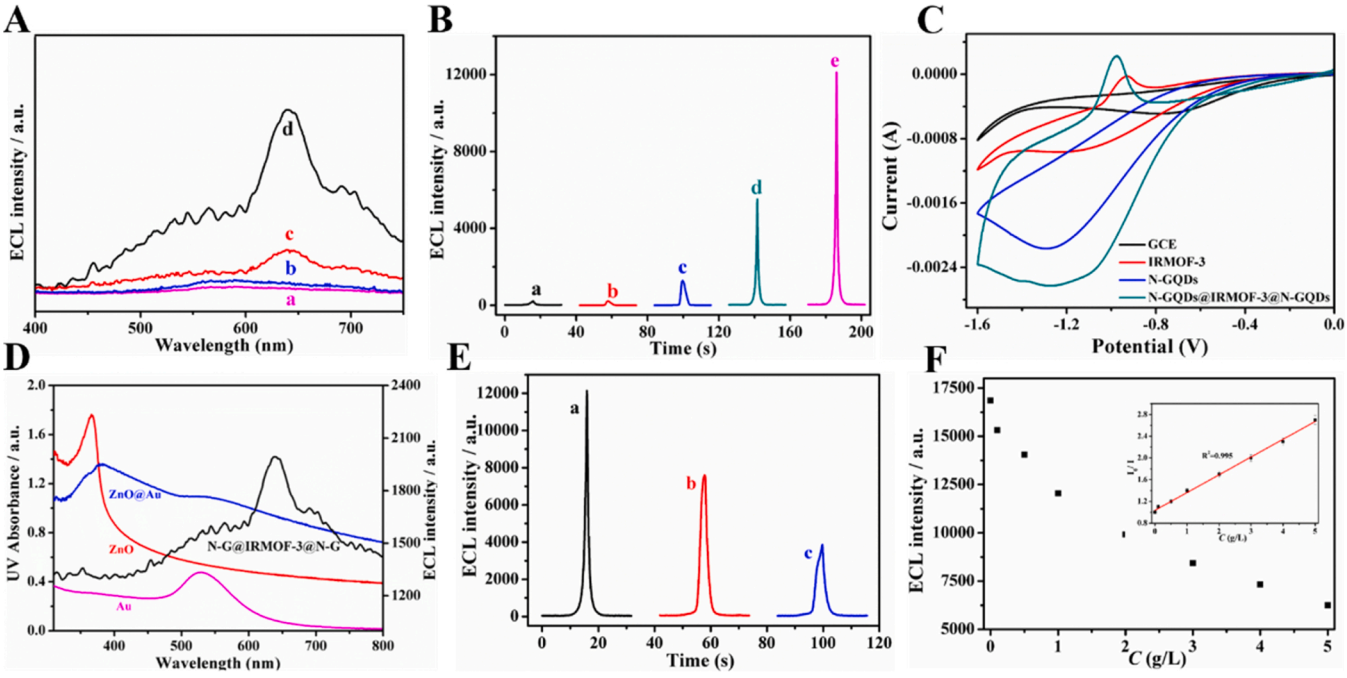

Fig. 2. (A) ECL emission spectra of GCE (a), IRMOF-3 (b), N-GQDs (c) and N-GQDs@IRMOF-3@N-GQDs (d) in PBS (pH 7.4, 0.1 M $K_2S_2O_8$) solution; (B) ECL responses of N-GQDs (a), N-GQDs@IRMOF-3 (b) in PBS (pH 7.4) solution. ECL responses of N-GQDs (c), N-GQDs@IRMOF-3 (d) and N-GQDs@IRMOF-3@N-GQDs (e) in PBS (pH 7.4, 0.1 M $K_2S_2O_8$) solution; (C) CV responses of GCE, IRMOF-3, N-GQDs and N-GQDs@IRMOF-3@N-GQDs in PBS (pH 7.4, 0.1 M $K_2S_2O_8$) solution; (D) UV–vis absorption of Au, ZnO, ZnO@Au and ECL emission spectrum of N-GQDs@IRMOF-3@N-GQDs; (E) ECL behavior of N-GQDs@IRMOF-3@N-GQDs (a), N-GQDs@IRMOF-3@N-GQDs/ZnO (b) and N-GQDs@IRMOF-3@N-GQDs/ZnO@Au (c); (F) ECL responses of N-GQDs@IRMOF-3@N-GQDs in the presence of 0, 0.1, 0.5, 1, 2, 3, 4 and 5 g L^{-1} ZnO@Au; The diagram inside corresponds to linear relationship.

The quenching mechanism between N-GQDs@IRMOF-3@N-GQDs and ZnO@Au was further studied. It can be seen from Fig. 2D that pure ZnO had a broad UV absorption spectrum, which partially overlapped with the ECL emission spectrum of N-GQDs@IRMOF-3@N-GQDs. This result indicated that the resonance energy transfer interaction could occur between N-GQDs@IRMOF-3@N-GQDs (donor) and ZnO@Au (acceptor) to quench the ECL signal. After surface modification of Au nanoparticles, the absorption peak of ZnO@Au became wider and the absorption intensity between 480 nm and 670 nm also increased, which further enhanced the overlap and quenching effect. And the corresponding ECL response was displayed in Fig. 2E. It can be observed that the combining of Au nanoparticles could enhance the quenching efficiency of ZnO. It can be demonstrated that ZnO@Au had dual-quenching effect to the ECL signal of N-GQDs@IRMOF-3@N-GQDs. To further investigate the performance of the ZnO@Au quencher, a series of concentrations of ZnO@Au (0, 0.1, 0.5, 1, 2, 3, 4 and 5 g L^{-1}) were used to quench the N-GQDs@IRMOF-3@N-GQDs. The ECL signal depicted in Fig. 2F gradually decreased when the concentration of quencher increased, and the corresponding linear relationship was shown inside of Fig. 2F in the range from 0 to 5.0 g L^{-1} ($R^2 = 0.995$). The quenching rate constant (k_q) was evaluated according to the Stern-Volmer equation: $I_0/I = 1 + k_q\tau_0[Q] = 1 + K_{sv}[Q]$ [71]. According to the fitted curve, the quenching constant (K_{SV}) was 3.268×10^5 g^{-1}. All the above results suggested the excellent dual-quenching effect of ZnO@Au.

3.3. Optimization of experimental conditions

The substrate concentration, co-reactant concentration, pH and quencher concentration were optimized based on the ECL strength and stability as the criterion to obtain the best testing efficiency of the constructed immunosensor. To achieve the highest ECL intensity, the concentration of the N-GQDs@IRMOF-3@N-GQDs was first selected. It can be seen from Fig. 3A, when the concentration of N-GQDs@IRMOF-3@N-GQDs was lower than 1.5 mg mL^{-1}, the ECL response and concentration were positively correlated. While the ECL response and concentration were negatively correlated when the concentration surpassed 1.5 mg mL^{-1}. So, the best concentration of N-GQDs@IRMOF-3@N-GQDs was defined as 1.5 mg mL^{-1}. Secondly, the concentration of $K_2S_2O_8$ was also optimized. Fig. 3B showed that the ECL response was primary increased with the increase of $K_2S_2O_8$ concentration before 100 mM, and then decreased. So, 100 mM of $K_2S_2O_8$ was selected as the test condition. Subsequently, the pH value of PBS was optimized. The pH value that too high or too low was not studied in the organism, so it was chosen to optimize in the pH range of 6.4–8.5. In Fig. 3C, when the pH value was 8.0, the ECL response reached the strongest, thus, the optimum pH value of PBS was 8.0. Finally, in order to achieve high-efficiency quenching effect, the concentration of ZnO@Au was selected. In Fig. 3D, the effect of quenching showed an upward trend when the concentration of ZnO@Au was below 2 mg mL^{-1}; when it was more than 2 mg mL^{-1}, the quenching effect was basically not changed. Hence, the best quenching concentration of ZnO@Au was defined as 2 mg mL^{-1}.

3.4. Characterization of the sensor

To explore the immunosensor construction process, different modified electrodes were studied by ECL intensity-potential measurement. In Fig. 4A, line a shown that a bare GCE in PBS (pH 8.0) containing 100 mM of $K_2S_2O_8$ had a weak ECL signal. ECL intensity was significantly enhanced after modification of N-GQDs@IRMOF-3@N-GQDs on the

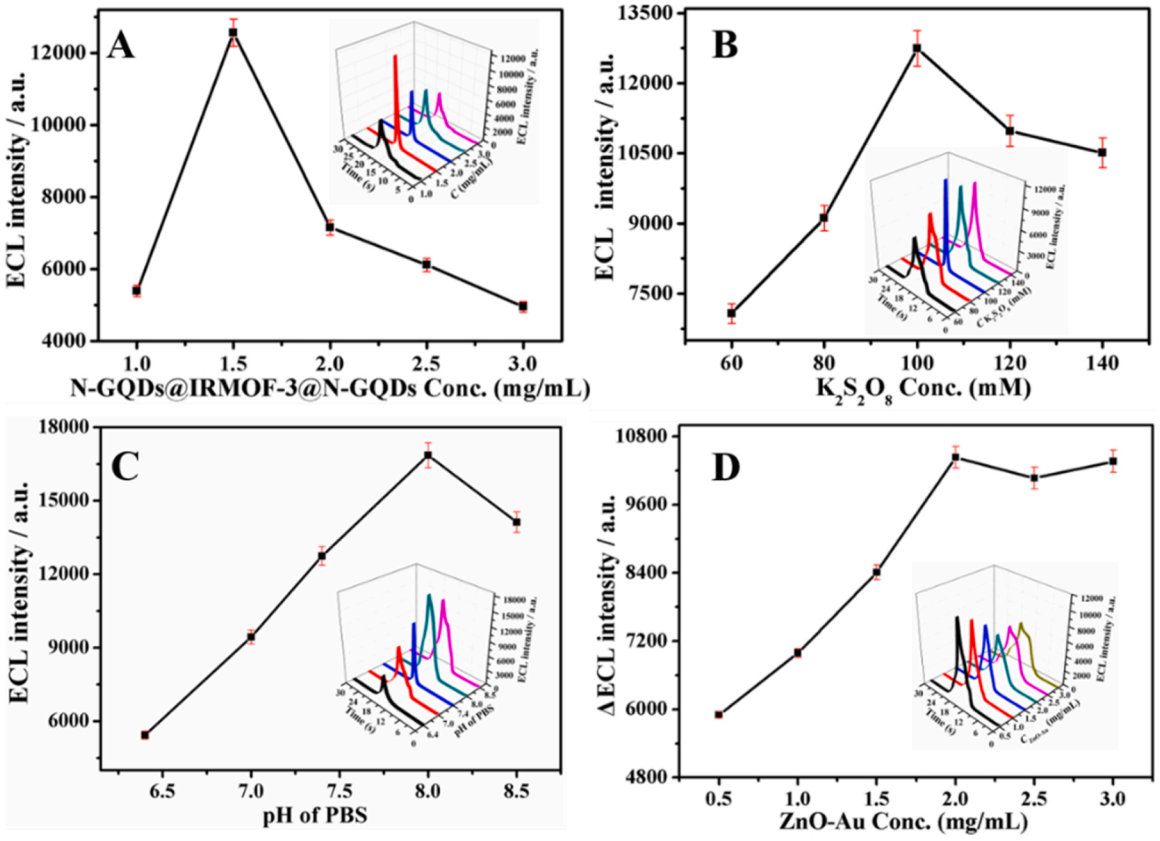

Fig. 3. The effect of concentration of N-GQDs@IRMOF-3@N-GQDs (A), concentration of $K_2S_2O_8$ (B), the pH of PBS (C) on the ECL response from GCE/N-GQDs@IRMOF-3@N-GQDs. (D) The quenching effect of different concentration of ZnO@Au on the ECL immunosensor for detection 0.01 ng mL^{-1} PCT (ΔECL intensity was the difference between GCE/N-GQDs@IRMOF-3@N-GQDs/Ab_1/BSA/PCT and GCE/N-GQDs@IRMOF-3@N-GQDs/Ab_1/BSA/PCT/ZnO@Au-Ab_2). The insert diagrams are the corresponded ECL-time curves. Error bars = RSD (n = 3).

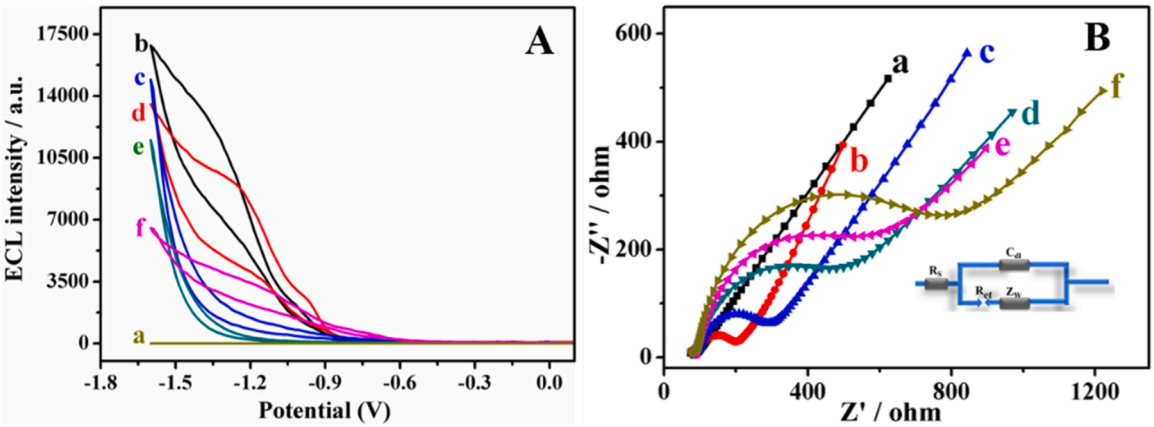

Fig. 4. (A) ECL-potential curves and (B) EIS curves of the proposed immunosensor: GCE (a), GCE/N-GQDs@IRMOF-3@N-GQDs (b), GCE/N-GQDs@IRMOF-3@N-GQDs/GCE/Ab_1(c), GCE/N-GQDs@IRMOF-3@N-GQDs/Ab_1/BSA (d), GCE/N-GQDs@IRMOF-3@N-GQDs/Ab_1/BSA/PCT (e), GCE/N-GQDs@IRMOF-3@N-GQDs/Ab_1/BSA/PCT/ZnO@Au-Ab_2 (f).

GCE (line b). The ECL intensity gradually decreased when Ab_1 (line c), BSA (line d) and PCT (line e) were added on the GCE surface step-by-step. This can be ascribed to that the electron transfer was blocked by these nonconducting protein molecules. When ZnO@Au-Ab_2 was finally incubated on the GCE (line f), the ECL response was minimized due to ECL inhibition of the quenching probe ZnO@Au-Ab_2. The above results manifested the successful construction of the immunosensor.

In addition, the construction process of the immunosensor was further illustrated by electrochemical impedance spectroscopy (EIS). Fig. 4B showed the EIS consequence of different modified states. The insert diagram at the lower right corner of Fig. 4B was an equivalent circuit. In detail, the bare electrode exhibited a tiny semicircle (line a), which represented the lowest electro-transfer resistance (R_{et}) and indicated the most free diffusion process of $[Fe(CN)_6]^{3-/4-}$ accessing modified electrode. When N-GQDs@IRMOF-3@N-GQDs was modified on the GCE, the semicircular domain was small (line b), suggesting that N-GQDs improved the conductivity of the composite material. The semicircular domain continued to increase when Ab_1 was modified on the electrode. Because Ab_1 acted as a non-conductive biological material blocked the electron transport (line c). When BSA (line d), PCT antigen (line e) continued to be modified, the semicircular domains continued to increase, indicating the above non-conductive biological substances have been successfully connected to the electrode. Finally, the semicircular domain was maximized when ZnO@Au-Ab_2 was modified, due to ZnO@Au-Ab_2 further hindered electron transport, proving the immune binding between antigen and Ab_2 biomarkers. It can be concluded according to the results above that the dual-quenching ECL immunosensor was successfully built. The corresponding values simulated by ZSimpWin software were shown in Table S1.

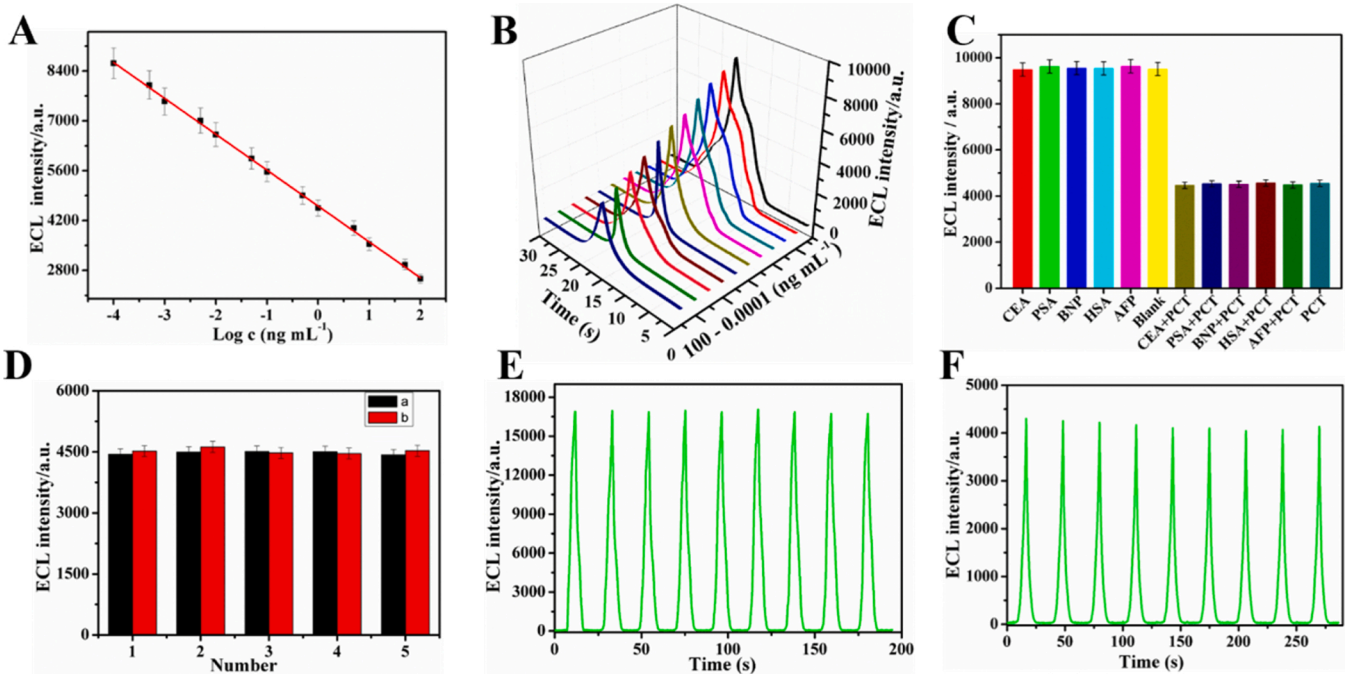

Fig. 5. The calibration curve (A) and ECL response (B) of the immunosensor to different concentrations of PCT: 0.0001, 0.0005, 0.001, 0.005, 0.01, 0.05, 0.1, 0.5, 1, 5, 10, 50 and 100 ng mL^{-1}; (C) Selectivity of the proposed ECL immunosensor in order: CEA (1 ng mL^{-1}), PSA (1 ng mL^{-1}), BNP (1 ng mL^{-1}), HSA (1 ng mL^{-1}), AFP (1 ng mL^{-1}), Blank, 1 ng mL^{-1} PCT with 100 ng mL^{-1} interference (CEA + PCT, PSA + PCT, BNP + PCT, HSA + PCT, AFP + PCT), and PCT (1 ng mL^{-1}); (D) The reproducibility of the immunosensor for 1 ng mL^{-1} PCT investigated by intra- (a) and inter-assay (b) precision. Error bars = RSD (n = 3); (E) Stability of GCE/N-GQDs@IRMOF-3@N-GQDs for 9 cycles; (F) Stability of the ECL immunosensor for 9 cycles. All were tested in 100 mM $K_2S_2O_8$ in PBS (pH = 8.0).

3.5. Analysis of PCT

To evaluate the detection property of incubated immunosensor under optimal conditions, the ECL responses were obtained by detecting PCT at a certain concentration. The ECL intensity to the corresponding concentrations and the simulated linear correlation curves were shown in Fig. 5A and B. When the PCT concentration increased from 0.0001 to 100 ng mL^{-1}, the ECL response showed a regular downward trend. The linear regression equation was $I_{ECL} = 4609.57 - 1007.48 \times \lg c$ ($R^2 = 0.998$) and the LOD was 12.58 fg mL^{-1} (S/N = 3). In addition, the comparison was made between this work and other reports (Table S2) to further illustrate the superiority of this method. The outstanding detection limit and detection range obtained in the end result might be due to the remarkable ECL property of N-GQDs@IRMOF-3@N-GQDs and excellent quenching performance of ZnO@Au.

3.6. Selectivity, repeatability, and stability of the immunosensor

Five common species in serum were selected as interfering substances, including carcinoembryonic antigen (CEA), prostate specific antigen (PSA), B-type natriuretic peptide (BNP), human serum albumin (HSA) and alpha fetoprotein (AFP) to evaluate the specificity of the constructed sensor. As shown in Fig. 5C, when detection object only contained 1 ng mL^{-1} of CEA, 1 ng mL^{-1} of PSA, 1 ng mL^{-1} of BNP, 1 ng mL^{-1} of HSA or 1 ng mL^{-1} of AFP, the ECL responses showed no obvious change when compared with the blank experimental. In addition, when the immunosensor was incubated with 1 ng mL^{-1} of PCT or the mixture of 1 ng mL^{-1} of PCT with 100 ng mL^{-1} of interference (CEA, PSA, BNP, HSA or AFP), the ECL responses were almost the same. In addition, more interferences such as ascorbic acid, uric acid, dopamine, cholesterol, myoglobin, serotonin and immunoglobulin, were further selected to evaluate the selectivity of the proposed sensor (Fig. S6 in Supplementary material). The above results indicated that the constructed sensor had acceptable selectivity.

Outstanding repeatability was an important factor for the immunosensor application. Therefore, inter- and intra-assay precision were investigated to test whether the reproducibility of the constructed sensor meets the requirements (Fig. 5D). Under the same experimental condition, the ECL responses of five electrodes in a same batch (cure a), and the same electrodes constructed in five batches (cure b) were analyzed, respectively. The RSD of intra- and inter-assay were 1.87 % and 2.39 %. The above results indicated that the constructed sensor had good reproducibility.

Stability was a major point for practical application of ECL immunosensor. N-GQDs@IRMOF-3@N-GQDs composites exhibited fairly stable ECL intensity under 9 consecutive scans (Fig. 5E), and the RSD was 0.644 %. Besides, the electrode modified with 5 ng mL^{-1} of PCT was scanned under consecutively potential (−1.6 V to 0 V) for 9 cycles, and the RSD was 2.21 % (Fig. 5F). The above results illustrated the construed immunosensor had acceptable stability.

3.7. Application of the fabricated ECL immunosensor in human serum

To further test the feasibility of the constructed sensor in PCT detection, recovery experiments were carried out in human serum samples by standard addition method. Herein, the serum was obtained from a local hospital and diluted 10 times before use. The PCT concentration of the diluted serum was measured to be 0.31 ng mL^{-1} by using immunosensor fabricated here (denoted as Detected concentration). Then the samples were divided into four groups, and each group was spiked with 0.05, 0.1, 0.5, 1 ng mL^{-1} of PCT standard samples, respectively (denoted as Added). After measurement, the corresponding PCT concentrations of these samples were obtained (denoted as Found). As listed in Table 1, the recoveries ranged from 96.8 % to 105.3 %, manifesting the developed immunosensor had satisfactory recovery and was expected to be used in practical detection.

Table 1
Recovery results of PCT in human serum samples detected by the proposed ECL biosensor.

Sample number	Detected concentration (ng mL^{-1})	Addition (ng mL^{-1})	Found (ng mL^{-1})	Recovery (%)	RSD (%, n = 3)
1	0.31	0.05	0.357	99.2	2.8
2	0.31	0.10	0.421	102.7	3.4
3	0.31	0.50	0.853	105.3	4.1
4	0.31	1.00	1.268	96.8	3.7

4. Conclusion

To sum up, a quenching ECL immunosensor on the basis of N-GQDs@IRMOF-3@N-GQDs as a new multifunctional luminescent substrate (donor) and ZnO@Au as a novel dual-quencher (acceptor) through ECL-RET interaction was firstly developed to realize ultrasensitive detection of PCT. In the current system, N-GQDs were firstly decorated on the inside and outside of the co-reaction accelerator IRMOF-3, which improved the load of luminous reagent and shortened the electron transmission distance, resulting in a high-efficiency signal probe N-GQDs@IRMOF-3@N-GQDs. Meanwhile, ZnO nanorods and Au nanoparticles were firstly combined to realize dual-quenching effect, which could greatly increase the sensitivity of the immunosensor. All in all, a wider linear detection range for PCT (0.0001–100 ng mL^{-1}), a lower detection limit of 12.58 fg mL^{-1} (S/N = 3), satisfactory sensitivity, specificity and reproducibility endowed this new sensing method potential application prospect in clinical diagnosis.

CRediT authorship contribution statement

Lihua Hu, Cui Song, Tengfei Shi and **Qin Wei** conceived and designed the experiments. **Cui Song** performed the experiments, analyzed the data and wrote the original draft of the manuscript. **Lihua Hu** analyzed the data and revised the manuscript. **Qianqian Cui, Lei Yang, Xiaojian Li, Dan Wu, Hongmin Ma, Yong Zhang** and **Huangxian Ju** contributed substantially to revisions. All the authors discussed the results and commented on the manuscript.

Declaration of Competing Interest

The authors declare that they have no known competing financial interests or personal relationships that could have appeared to influence the work reported in this paper.

Acknowledgements

This study was supported by the National Key Scientific Instrument and Equipment Development Project of China (No. 21627809), National Natural Science Foundation of China (Nos. 21607055, 21675063, 21775054, 21505051, 21575050, 21777056, 21427808).

Appendix A. Supplementary data

Supplementary material related to this article can be found, in the online version, at doi:https://doi.org/10.1016/j.snb.2021.130495.

References

[1] Y. Li, W. Liu, G. Jin, Y. Niu, Y. Chen, M. Xie, Label-free sandwich imaging ellipsometry immunosensor for serological detection of procalcitonin, Anal. Chem. 90 (2018) 8002–8010.
[2] W.J. Shen, Y. Zhuo, Y.Q. Chai, Z.H. Yang, J. Han, R. Yuan, Enzyme-free electrochemical immunosensor based on host–guest nanonets catalyzing amplification for procalcitonin detection, ACS Appl. Mater. Interfaces 7 (2015) 4127–4134.

[3] C.Y. Chiang, T.T. Huang, C.H. Wang, C.J. Huang, T.H. Tsai, S.N. Yu, et al., Fiber optic nanogold-linked immunosorbent assay for rapid detection of procalcitonin at femtomolar concentration level, Biosens. Bioelectron. 151 (2020), 111871.

[4] Y. Li, L. Liu, X. Liu, Y. Ren, K. Xu, N. Zhang, et al., A dual-mode PCT electrochemical immunosensor with $CuCo_2S_4$ bimetallic sulfides as enhancer, Biosens. Bioelectron. 163 (2020), 112280.

[5] T. Lisboa, J. Salluh, P. Povoa, Do we need new trials of procalcitonin-guided antibiotic therapy? Crit. Care 22 (2018) 1–3.

[6] M.A. Meier, A. Branche, O.L. Neeser, Y. Wirz, S. Haubitz, L. Bouadma, et al., Procalcitonin-guided antibiotic treatment in patients with positive blood cultures: a patient-level meta-analysis of randomized trials, Clin. Infect. Dis. 69 (2019) 388–396.

[7] Julie Davies, Procalcitonin, J. Clin. Pathol. 68 (2015) 675–679.

[8] O. Burkhardt, S. Ewig, U. Haagen, S. Giersdorf, O. Hartmann, K. Wegscheider, et al., Procalcitonin guidance and reduction of antibiotic use in acute respiratory tract infection, Eur. Respir. J. 36 (2010) 601–607.

[9] D.N. Bremmer, M.A. Moffa, K. Ma, H.R. Bean, J. Snatchko, T.L. Trienski, et al., Acute exacerbations of chronic obstructive pulmonary disease with a low procalcitonin concentration: impact of antibiotic therapy, Clin. Infect. Dis. 68 (2019) 725–730.

[10] X.Y. Shao, C. R.Wang, C.M. Xie, X.G. Wang, R.L. Liang, W.W. Xu, Rapid and sensitive lateral flow immunoassay method for procalcitonin (PCT) based on time-resolved immunochromatography, Sensors 17 (2017) 480, https://doi.org/10.3390/s17030480.

[11] Z. Yang, X. Shao, Y. Han, H. Zhang, Detection of procalcitonin (PCT) using the double antibody sandwich method based on fluorescence resonance energy transfer between upconversion nanoparticles and quantum dots, Anal. Methods 10 (2018) 1015–1022.

[12] X. Zhang, H. Meng, X. Sun, L. Xu, L. Zhang, D. Shi, X. Feng, R. Lu, Z. Chen, Elevation of vitamin D-binding protein levels in the plasma of patients with generalized aggressive periodontitis, J. Periodont. Res. 48 (2013) 74–79.

[13] Y. Wu, L. Liu, Z. Liang, Z. Shen, X. Zhu, Colorimetric and electrochemical study on the interaction between gold nanoparticles and unmodified DNA, Curr. Nanosci. 7 (2011) 359–365.

[14] H. Ke, H. Sha, Y. Wang, W. Guo, X. Zhang, Z. Wang, et al., Electrochemiluminescence resonance energy transfer system between GNRs and $Ru(bpy)_3^{2+}$: application in magnetic aptasensor for β-amyloid, Biosens. Bioelectron. 100 (2018) 266–273.

[15] Z. Li, Z. Lin, X. Wu, H. Chen, Y. Chai, R. Yuan, Highly efficient electrochemiluminescence resonance energy transfer system in one nanostructure: its application for ultrasensitive detection of microRNA in cancer cells, Anal. Chem. 89 (2017) 6029–6035.

[16] H.J. Lu, J.B. Pan, Y.Z. Wang, S.Y. Ji, W. Zhao, X.L. Luo, et al., Electrochemiluminescence energy resonance transfer system between RuSi nanoparticles and hollow Au nanocages for nucleic acid detection, Anal. Chem. 90 (2018) 10434–10441.

[17] X.L. Fu, F. Hou, F.R. Liu, S.W. Ren, J.T. Cao, Y.M. Liu, Electrochemiluminescence energy resonance transfer in 2D/2D heterostructured g-C_3N_4/MnO_2 for glutathione detection, Biosens. Bioelectron. 129 (2019) 72–78.

[18] M.S. Wu, L.J. He, J.J. Xu, H.Y. Chen, RuSi@$Ru(bpy)_3^{2+}$/Au@Ag_2S nanoparticles electrochemiluminescence resonance energy transfer system for sensitive DNA detection, Anal. Chem. 86 (2014) 4559–4565.

[19] X.L. Huo, N. Zhang, H. Yang, J.J. Xu, H.Y. Chen, Electrochemiluminescence resonance energy transfer system for dual-wavelength ratiometric miRNA detection, Anal. Chem. 90 (2018) 13723–13728.

[20] B. Babamiri, A. Salimi, R. Hallaj, Switchable electrochemiluminescence aptasensor coupled with resonance energy transfer for selective attomolar detection of Hg^{2+} via CdTe@CdS/dendrimer probe and Au nanoparticle quencher, Biosens. Bioelectron. 102 (2018) 328–335.

[21] R. Zhang, J.R. Adsetts, Y. Nie, X. Sun, Z. Ding, Electrochemiluminescence of nitrogen- and sulfur-doped graphene quantum dots, Carbon 129 (2018) 45–53.

[22] P. Li, C. Wu, Y. Xu, D. Cheng, Q. Lu, J. Gao, et al., Group IV nanodots: newly emerging properties and application in biomarkers sensing, TrAC Trends Anal. Chem. 131 (2020), 116007.

[23] X. Yan, X. Cui, L.-s. Li, Synthesis of large, stable colloidal graphene quantum dots with tunable size, J. Am. Chem. Soc. 132 (2010) 5944–5945.

[24] L. Lin, X. Song, Y. Chen, M. Rong, T. Zhao, Y. Jiang, et al., One-pot synthesis of highly greenish-yellow fluorescent nitrogen-doped graphene quantum dots for pyrophosphate sensing via competitive coordination with Eu^{3+} ions, Nanoscale 7 (2015) 15427–15433.

[25] M.F. Sun, J.L. Liu, Y. Zhou, J.Q. Zhang, Y.Q. Chai, Z.H. Li, et al., High-efficient electrochemiluminescence of bcno quantum dot-equipped boron active sites with unexpected catalysis for ultrasensitive detection of microrna, Anal. Chem. 92 (2020) 14723–14729.

[26] N.A. Travlou, D.A. Giannakoudakis, M. Algarra, A.M. Labella, E. Rodríguez-Castellón, T.J. Bandosz, S- and N-doped carbon quantum dots: surface chemistry dependent antibacterial activity, Carbon 135 (2018) 104–111.

[27] B. Shi, Y. Su, L. Zhang, M. Huang, X. Li, S. Zhao, Facilely prepared Fe_3O_4/nitrogen-doped graphene quantum dot hybrid as a robust nonenzymatic catalyst for visual discrimination of phenylenediamine isomers, Nanoscale 8 (2016) 10814–10822.

[28] Y. Xu, P. Li, D. Cheng, C. Wu, Q. Lu, W. Yang, et al., Group IV nanodots: synthesis, surface engineering and application in bioimaging and biotherapy, J. Mater. Chem. B 8 (2020) 10290–10308.

[29] D. Li, J. Fan, X. Wang, Preparation of N-doped graphene quantum dots and their photocatalytic degradation activity for methylene blue, Carbon 104 (2016) 261.

[30] B. Hui, W. Qian, Y. Siwei, Y. Changjie, W. Haoran, L. Lei, et al., Nitrogen-doped graphene quantum dots for 80% photoluminescence quantum yield for inorganic γ-$CsPbI_3$ perovskite solar cells with efficiency beyond 16%, J. Mater. Chem. A 7 (2019) 5740–5747.

[31] B.M. Mark, B.S. Tyler, L.K. Emily, G.M. Joseph, S.S. Dwight, Electrochemical polymerization of functionalized graphene quantum dots, Chem. Mater. 29 (2017) 6611–6615.

[32] Y. Xuan, R.Y. Zhang, D.H. Zhao, X.S. Zhang, J. An, K. Cheng, et al., Ultrafast synthesis of gold nanosphere cluster coated by graphene quantum dot for active targeting PA/CT imaging and near-infrared laser/pH-triggered chemo-photothermal synergistic tumor therapy, Chem. Eng. J. 369 (2019) 87–99.

[33] S. Chen, X. Chen, T. Xia, Q. Ma, A novel electrochemiluminescence sensor for the detection of nitroaniline based on the nitrogen-doped graphene quantum dots, Biosens. Bioelectron. 85 (2016) 903–908.

[34] H. Yuan, J. Yu, S. Feng, Y. Gong, Highly photoluminescent pH-independent nitrogen-doped carbon dots for sensitive and selective sensing of p-nitrophenol, RSC Adv. 6 (2016) 15192–15200.

[35] Q. Li, S. Zhang, L. Dai, L. Li, Nitrogen-doped colloidal graphene quantum dots and their size-dependent electrocatalytic activity for the oxygen reduction reaction, J. Am. Chem. Soc. 134 (2012) 18932–18935.

[36] Z. Zeng, F.X. Xiao, G.F. Gui, R. Wang, B. Liu, T.T.Y. Tan, Layer-by-layer of nitrogen-doped graphene quantum dots monolayer decorated one-dimensional semiconductor nanoarchitectures for solar-driven water splitting, J. Mater. Chem. A 4 (2016) 16383–16393.

[37] X. Zou, M. Liu, J. Wu, P.M. Ajayan, J. Li, B. Liu, et al., How the nitrogen-doped graphene quantum dots catalyze electroreduction of CO_2 to hydrocarbons and oxygenates, ACS Catal. 7 (2017) 6245–6250.

[38] Y. Yang, Q. Liu, Y. Liu, J. Cui, H. Liu, P. Wang, et al., A novel label-free electrochemical immunosensor based on functionalized nitrogen-doped graphene quantum dots for carcinoembryonic antigen detection, Biosens. Bioelectron. 90 (2017) 31–38.

[39] W. Zhu, M. Saddam Khan, W. Cao, X. Sun, H. Ma, Y. Zhang, et al., $Ni(OH)_2$/NGQDs-based electrochemiluminescence immunosensor for prostate specific antigen detection by coupling resonance energy transfer with Fe_3O_4@MnO_2 composites, Biosens. Bioelectron. 99 (2018) 346–352.

[40] S. Zuluaga, E.M.A. Fuentes-Fernandez, K. Tan, F. Xu, J. Li, Y.J. Chabal, et al., Understanding and controlling water stability of MOF-74, J. Mater. Chem. A 4 (2016) 5176–5183.

[41] Y. Gu, Yn. Wu, L. Li, W. Chen, F. Li, S. Kitagawa, Controllable modular growth of hierarchical MOF-on-MOF architectures, Angew. Chemie Int. Ed. 129 (2017) 15864–15868.

[42] Y. Sun, Y. Zhang, H. Zhang, M. Liu, Y. Liu, Integrating highly efficient recognition and signal transition of g-C_3N_4 embellished Ti_3C_2 MXene hybrid nanosheets for electrogenerated chemiluminescence analysis of protein kinase activity, Anal. Chem. 92 (2020) 10668–10676.

[43] X. Liu, M. Hu, M. Wang, Y. Song, N. Zhou, L. He, et al., Novel nanoarchitecture of Co-MOF-on-TPN-COF hybrid: ultralowly sensitive bioplatform of electrochemical aptasensor toward ampicillin, Biosens. Bioelectron. 123 (2019) 59–68.

[44] N. Zhou, Y. Ma, B. Hu, L. He, S. Wang, Z. Zhang, et al., Construction of Ce-MOF@COF hybrid nanostructure: label-free aptasensor for the ultrasensitive detection of oxytetracycline residues in aqueous solution environments, Biosens. Bioelectron. 127 (2019) 92–100.

[45] H. Bux, C. Chmelik, R. Krishna, J. Caro, Ethene/ethane separation by the MOF membrane ZIF-8: molecular correlation of permeation, adsorption, diffusion, J. Memb. Sci. 369 (2011) 284–289.

[46] K.J. Hartlieb, J.M. Holcroft, P.Z. Moghadam, N.A. Vermeulen, M.M. Algaradah, M. S. Nassar, et al., CD-MOF: a versatile separation medium, J. Am. Chem. Soc. 138 (2016) 2292–2301.

[47] K. Deng, Z. Hou, X. Li, C. Li, Y. Zhang, X. Deng, et al., Aptamer-mediated up-conversion core/MOF shell nanocomposites for targeted drug delivery and cell imaging, Sci. Rep. 5 (2015) 7851.

[48] M.X. Wu, Y.W. Yang, Metal–organic framework (MOF)-based drug/cargo delivery and cancer therapy, Adv. Mater. 29 (2017), 1606134.

[49] X. Wang, J. Zhou, H. Fu, W. Li, X. Fan, G. Xin, et al., MOF derived catalysts for electrochemical oxygen reduction, J. Mater. Chem. A 2 (2014) 14064–14070.

[50] M. Kalaj, M.S. Denny Jr., K.C. Bentz, J.M. Palomba, S.M. Cohen, Nylon–MOF composites through postsynthetic polymerization, Angew. Chemie Int. Ed. 131 (2019) 2358–2362.

[51] X. Zhu, H. Zheng, X. Wei, Z. Lin, L. Guo, B. Qiu, et al., Metal–organic framework (MOF): a novel sensing platform for biomolecules, Chem. Commun. 49 (2013) 1276–1278.

[52] H.Y. Li, Y.L. Wei, X.Y. Dong, S.Q. Zang, T.C. Mak, Novel Tb-MOF embedded with viologen species for multi-photofunctionality: photochromism, photomodulated fluorescence, and luminescent pH sensing, Chem. Mater. 27 (2015) 1327–1331.

[53] J.M. Yang, Q. Liu, Y.S. Kang, W.Y. Sun, Controlled growth and gas sorption properties IRMOF-3 nano/microcrystals, Dalton Trans. 43 (2014) 16707–16712.

[54] S. Banerjee, S.C. Pillai, P. Falaras, K.E. O'shea, J.A. Byrne, D.D. Dionysiou, New insights into the mechanism of visible light photocatalysis, J. Phys. Chem. Lett. 5 (2014) 2543–2554.

[55] S. Sood, A. Umar, S.K. Mehta, S.K. Kansal, Highly effective Fe-doped TiO_2 nanoparticles photocatalysts for visible-light driven photocatalytic degradation of toxic organic compounds, J. Colloid Interface Sci. 450 (2015) 213–223.

[56] A. Zielińska-Jurek, E. Kowalska, J.W. Sobczak, W. Lisowski, B. Ohtani, A. Zaleska, Preparation and characterization of monometallic (Au) and bimetallic (Ag/Au) modified-titania photocatalysts activated by visible light, Appl. Catal. B: Environ. 101 (2011) 504–514.

[57] E. Casals, T. Pfaller, A. Duschl, G.J. Oostingh, V.F. Puntes, Hardening of the nanoparticle–protein corona in metal (Au, Ag) and oxide (Fe_3O_4, CoO, and CeO_2) nanoparticles, Small 7 (2011) 3479–3486.
[58] J. Du, J. Qi, D. Wang, Z. Tang, Facile synthesis of Au@TiO_2 core–shell hollow spheres for dye-sensitized solar cells with remarkably improved efficiency, Energy Environ. Sci. 5 (2012) 6914–6918.
[59] A. Ayati, A. Ahmadpour, F.F. Bamoharram, B. Tanhaei, M. Mänttäri, M. Sillanpää, A review on catalytic applications of Au/TiO_2 nanoparticles in the removal of water pollutant, Chemosphere 107 (2014) 163–174.
[60] J. Guo, J. Zhang, M. Zhu, D. Ju, H. Xu, B. Cao, High-performance gas sensor based on ZnO nanowires functionalized by Au nanoparticles, Sens. Actuators B: Chem. 199 (2014) 339–345.
[61] X. Liu, J. Iocozzia, Y. Wang, X. Cui, Y. Chen, S. Zhao, et al., Noble metal–metal oxide nanohybrids with tailored nanostructures for efficient solar energy conversion, photocatalysis and environmental remediation, Energy Environ. Sci. 10 (2017) 402–434.
[62] G. Zhao, Y. Wang, X. Li, X. Dong, H. Wang, B. Du, et al., Quenching electrochemiluminescence immunosensor based on resonance energy transfer between ruthenium (ii) complex incorporated in the UiO-67 metal–organic framework and gold nanoparticles for insulin detection, ACS Appl. Mater. Interfaces 10 (2018) 22932–22938.
[63] S. Senthilkumar, M.S. Maru, R.S. Somani, H.C. Bajaj, S. Neogi, Unprecedented NH_2-MIL-101(Al)/n-Bu_4NBr system as solvent-free heterogeneous catalyst for efficient synthesis of cyclic carbonates via CO_2 cycloaddition, Dalton Trans. 47 (2018) 418–428.
[64] Y. Yoo, V. Varela-Guerrero, H.K. Jeong, Isoreticular metal-organic frameworks and their membranes with enhanced crack resistance and moisture stability by surfactant-assisted drying, Langmuir 27 (2011) 2652–2657.
[65] M. Zhao, K. Deng, L. He, Y. Liu, G. Li, H. Zhao, et al., Core–shell palladium nanoparticle@metal–organic frameworks as multifunctional catalysts for cascade reactions, J. Am. Chem. Soc. 136 (2014) 1738–1741.
[66] X. Pang, Y. Zhang, C. Liu, Y. Huang, Y. Wang, J. Pan, et al., Enhanced photoelectrochemical cytosensing of fibroblast-like synoviocyte cells based on visible light-activated ox-GQDs and carboxylated g-C_3N_4 sensitized TiO_2 nanorods, J. Mater. Chem. B 4 (2016) 4612–4619.
[67] L. Liu, X. Zhang, J. Gao, C. Xu, Engineering metal-organic frameworks immobilize gold catalysts for highly efficient one-pot synthesis of propargylamines, Green Chem. 14 (2012) 1710–1720.
[68] B. Cheng, E.T. Samulski, Hydrothermal synthesis of one-dimensional ZnO nanostructures with different aspect ratios, Chem. Commun. (2004) 986–987.
[69] Y.M. Lei, W.X. Huang, M. Zhao, Y.Q. Chai, R. Yuan, Y. Zhuo, Electrochemiluminescence resonance energy transfer system: mechanism and application in ratiometric aptasensor for lead ion, Anal. Chem. 87 (2015) 7787–7794.
[70] H. Peng, Z. Huang, H. Deng, W. Wu, K. Huang, Z. Li, et al., Dual enhancement of gold nanocluster electrochemiluminescence: electrocatalytic excitation and aggregation-induced emission, Angew. Chemie Int. Ed. 132 (2020) 10068–10071.
[71] J. Xue, L. Yang, Y. Jia, Y. Zhang, D. Wu, H. Ma, et al., Dual-quenching electrochemiluminescence resonance energy transfer system from Ru–In_2S_3 to α-MoO_3-Au based on protect of protein bioactivity for procalcitonin detection, Biosens. Bioelectron. 142 (2019), 111524.

Lihua Hu received her Ph.D. degree from University of science and technology of China in 2011. Now, she is an associate professor at University of Jinan. Her main research interests focus on the determination of biological targets through chemical sensors.

Cui Song studies in school of chemistry and chemical engineering, University of Jinan as postgraduate student.

Tengfei Shi studies in school of chemistry and chemical engineering, University of Jinan as postgraduate student.

Qianqian Cui studies in school of chemistry and chemical engineering, University of Jinan as postgraduate student.

Lei Yang studies in school of chemistry and chemical engineering, University of Jinan as doctoral student.

Xiaojian Li studies in school of chemistry and chemical engineering, University of Jinan as doctoral student.

Dan Wu received the D.S. degree from Shandong University in 2005. Now, she is a professor at University of Jinan. She dedicates to the surfactant and biological macromolecules interaction. And now she also studies the role of surfactant in electrochemical immunosensor.

Hongmin Ma received both his B.S. and M.S. degree in Applied Chemistry from University of Jinan in 2005 and 2008 respectively. And he has received his Ph.D. degree in Colloid and Interface Chemistry at Shandong University, investigating self-assembly at all scales at surfaces in 2011. Now, he is a professor at University of Jinan, interested in the assembly of nano-composites and the construction of ordered porous films as well as their analytical applications.

Yong Zhang received his B.S. degree in applied chemistry from University of Jinan in 2001, M.S. degree in applied chemistry from Nanjing University of Technology in 2005 and Ph.D. degree in Beijing Institute of Technology in 2016. Now, he is an associate professor at University of Jinan. His main research interests are chemical sensors and biosensors.

Qin Wei, a professor and DSc, has devoted herself to analytical teaching and scientific research. Her main research interests are the determination of protein and nucleic acid by photometry and the electrochemical immunosensor preparation. She has published over one hundred articles on analysis, immunosensor and applied successfully for many research projects, such as *Biomaterials, Adv. Funct. Mater., Biosens. Bioelectron., Sens. Actuators B: Chem., Talanta.*

Huangxian Ju received his BS, MS and Ph.D. degrees from Nanjing University during 1982–1992. He was a postdoc in Montreal University (Canada) from 1996 to 1997 and a guest professor in three universities of Germany and Ireland in 1999−2000. He became an associate and full professor of Nanjing University in 1993 and 1999. He is currently the director of State Key Laboratory of Analytical Chemistry for Life Science. His research interests focus on analytical biochemistry, biosensing and molecular diagnosis. He has published 616 papers in different journals with SCI h-index of 83 (29,523 citations) and Google Scholar h-index of 91 with more than 29000 citations.